

Multi-Wheeled Passive Sliding with Fully-Actuated Aerial Robots: Tip-Over Recovery and Avoidance

Tong Hui^{1*}, Eugenio Cuniato², Michael Pantic², Jefferson Ghielmini², Christian Lanegger², Dimitrios Papageorgiou¹, Marco Tognon³, Roland Siegwart², Matteo Fumagalli¹

¹ Department of Electrical and Photonics Engineering, Technical University of Denmark, Denmark

² Autonomous Systems Lab, ETH Zurich, Switzerland

³ Univ Rennes, CNRS, Inria, IRISA, F-35000 Rennes, France

*Corresponding author email: tonhu@dtu.dk

Abstract—Push-and-slide tasks carried out by fully-actuated aerial robots can be used for inspection and simple maintenance tasks at height, such as non-destructive testing and painting. Often, an end-effector based on multiple non-actuated contact wheels is used to contact the surface. This approach entails challenges in ensuring consistent wheel contact with a surface whose exact orientation and location might be uncertain due to sensor aliasing and drift. Using a standard full-pose controller dependent on the inaccurate surface position and orientation may cause wheels to lose contact during sliding, and subsequently lead to robot tip-over. To address the tip-over issue, we present two approaches: (1) tip-over avoidance guidelines for hardware design, and (2) control for tip-over recovery and avoidance. Physical experiments with a fully-actuated aerial vehicle were executed for a push-and-slide task on a flat surface. The resulting data is used in deriving tip-over avoidance guidelines and designing a simulator that closely captures real-world conditions. We then use the simulator to test the effectiveness and robustness of the proposed approaches in risky scenarios against uncertainties.

I. INTRODUCTION

With the growing interest in utilizing aerial robots for industrial applications, there has been a notable increase in research dedicated to aerial systems engaging in physical interactions with the environment over the past decade. The aerial robotic community is actively researching diverse physical interaction tasks [15], with a primary goal of broadening the range of potential industrial applications. Furthermore, push-and-slide tasks are of particular interest thanks to their applicability in several use cases, e.g., continuous scanning for Non-Destructive Testing (NDT) [25, 26, 31, 13, 27, 6] such as ultrasonic testing, layouting [10, 2], cleaning and grinding [28].

The physical contact for different interaction tasks between the robot and the environment is in general achieved through specialized end-effectors. A range of different types of end-effectors with variable contact points has been studied in current literature for push-and-slide tasks involving non-wheeled and wheeled designs. In [12, 30, 19], non-wheeled end-effectors with one contact point are tested. With these end-effectors, the system has to overcome the static friction to start a sliding motion. This often causes a sudden acceleration in the system due to the switch from static to dynamic friction. Moreover, the static and dynamic friction coefficients vary

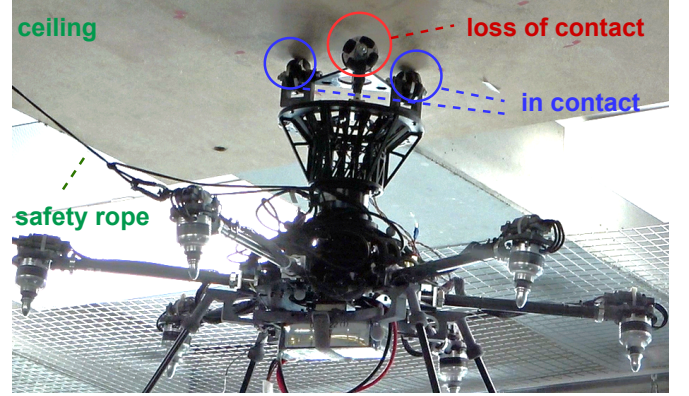


Fig. 1: Image of a tip-over during a passive sliding task with a fully-actuated aerial vehicle. For the full action, please see the attached video. The aerial vehicle is equipped with three omniwheels at the end-effector tip. A wooden board is mounted on the ceiling as the work surface to be slid on. In this tip-over image, two wheels (marked with blue circles) are in contact with the work surface while one (marked with a red circle) loses contact. A safety rope is used to reduce platform damage in risky scenarios.

on different work surfaces [29]. Therefore, non-wheeled end-effectors are not the best for sliding tasks considering diverse testing conditions. In [2, 26, 27], a one-wheeled end-effector is used which also has one contact point but is more widely used for sliding motions thanks to the wheel's rolling ability. However, wheeled end-effectors with only one contact point hinder the placement of additional equipment e.g., sensors and tools, which limits the application range of the robot. In this paper, we refer to systems equipped with more than one wheel as *multi-wheeled systems*, e.g., *three-wheeled systems*, *four-wheeled systems*. In [28, 31, 10, 6], three-wheeled and four-wheeled end-effectors with multiple contact points are implemented which allow for the mounting of tools and sensors in the middle of the end-effector tip. While a multi-wheeled end-effector is sliding on the work surface, one of the main objectives is to ensure stable contact between all wheels of the end-effector and the work surface [15].

We define the use of actuated wheels as *active sliding*, and the use of non-actuated wheels as *passive sliding*. Wopereis et al. [28], Lanegger et al. [10], and Hui et al. [6] demonstrate multi-wheeled active sliding with underactuated as well as

fully-actuated aerial vehicles on flat surfaces. Active sliding imposes relatively simple control requirements on the aerial system to ensure stable contact between wheels and the work surface during sliding [6]. Moreover, the sliding motion is driven directly by the wheel motors. Despite the simple control requirements of active sliding, the addition of wheel motors often leads to bulky end-effector designs and additional weight. Zhao et al. [31] presents passive sliding with a four-wheeled end-effector and showcases the operation in simulations. However, there is still a lack of studies that focus on physical effects and crucial contact conditions during passive sliding with aerial robots. In aerial systems, there are common systematic uncertainties caused by modeling errors in thrust estimation, Center of Mass (CoM) offsets, and sensor noise. The effects of these uncertainties are often neglected for free flight, however, they can be critical for multi-wheeled passive sliding tasks which require full contact among all wheels and the work surface. Even small errors in the orientation of the system can cause loss of contact between the wheels and the work surface, known as *tip-over issue* in wheeled locomotion [23], occasionally even leading to system instability. As an example, a tip-over scene during a push-and-slide task with a three-wheeled aerial vehicle is shown in Fig. 1. In this tip-over situation, only two out of three wheels are in contact with the work surface. During passive sliding, only the propulsion system of the aerial vehicle provides the necessary forces and torques (i.e., wrenches) needed for the sliding motion as well as the contact keeping.

A. Critical issues in multi-wheeled passive sliding with fully-actuated aerial vehicles

Compared to regular 4-Degree of Freedom (DoF) quadrotors, fully-actuated aerial vehicles enable stable 6-DoF force and torque exertion for aerial manipulation [21]. The 6-DoF wrench generation capability is often realized using either fixed tilted propellers [20, 14, 24, 18] or actively tiltable propellers [27, 9, 7, 8, 2]. The most common control methods for tilt-rotor aerial vehicles in physical interactions are impedance control and hybrid motion/force control [15]. Between them, impedance control is more widely used since switching controllers between free-flight and interactions can be avoided [15]. For multi-wheeled passive sliding on an unknown surface using fully-actuated aerial vehicles with 6-DoF impedance control as in [27, 2], attitude errors caused by systematic uncertainties and inaccurate attitude references could lead to initial misalignment between the end-effector tip and the work surface. Moreover, the wheel contact during sliding is not guaranteed. Both issues lead to robot tip-over as in Fig. 1. The tip-over at initial contact is usually resolved by manually slowly adjusting the aerial vehicle orientation which is time-consuming and might lead to instability due to human errors. The tip-over during sliding often leads to low-quality measurements in NDT or low-precision operations in other applications. The outlined challenges motivate a more in-depth investigation into theoretical tip-over stability conditions for push-and-slide applications with fully-actuated aerial vehicles.

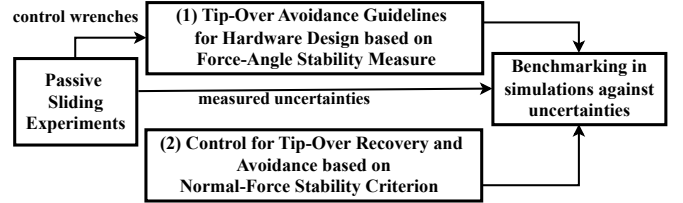


Fig. 2: The work scope of this article. Physical experiments of passive sliding were conducted featuring the tip-over issue and two approaches are proposed to resolve the tip-over issue.

II. RELATED WORK

The tip-over problem has been broadly studied for over twenty years on mobile robots and several tip-over stability criteria are developed. Sugano et al. [23] and Huang et al. [5] presented the Zero Momentum Point (ZMP) criterion-based tip-over stability measure for mobile manipulators, which cannot tackle the change of CoM. Ghasempoor and Sepehri [4] reported the energy-based stability criterion which has the risk of real-time instability due to its complex computation [3]. A. Moosaviani and Alipour [1] introduced the moment-height tip-over stability measure which requires the computation of the moment of inertia concerning each side of the support polygon. Papadopoulos and Rey [16] [17] presented the force-angle tip-over stability measure which captures the change of CoM in contrast to the ZMP criterion and is easy to compute.

Among the aforementioned tip-over stability criteria, the force-angle stability measure requires relatively low computation cost and is effective in tip-over prediction for mobile manipulators. However, considering aerial systems which are often subjected to more systematic uncertainties and higher risk of real-time instability compared to mobile robots, the effectiveness of the force-angle stability measure on fully-actuated aerial systems needs further investigation. Liu and Liu [11] introduced a normal-force-based tip-over stability criterion which can explicitly measure the tip-over stability using force sensors. The criterion is then used for online tip-over prevention by limiting the system motion. And yet, in wheeled mobile manipulator studies, there is a lack of active control approaches that help the system recover from tip-overs and actively generate control wrenches to avoid tip-overs even during sliding maneuvers. This is because the wheeled mobile manipulators often do not have full actuation in 6-DoF. Fully-actuated aerial systems, however, offer such capabilities. Moreover, the normal forces can be measured with only pressure sensors attached to wheels at a low cost, and the associated stability criterion is straightforward to implement which makes it a good candidate for tip-over control.

III. MAIN CONTRIBUTION

In this paper, we aim to resolve the tip-over issues for multi-wheeled passive sliding with fully-actuated aerial vehicles on unknown flat surfaces with effective, economical, and easy-to-adapt solutions. Inspired by the related work on mobile manipulators, we propose two approaches for the identified issues from both hardware design and control perspectives:

- 1) the establishing of tip-over avoidance guidelines for hardware design based on an off-line force-angle tip-over stability measure;
- 2) a novel controller for tip-over recovery and avoidance based on the normal-force tip-over stability criterion.

The work scope of this article is displayed in Fig. 2. Physical experiments with a fully-actuated aerial vehicle were executed for a push-and-slide task on a flat surface. The control wrenches from resulting data are used for deriving tip-over avoidance guidelines of approach (1), and the measured uncertainties during experiments are used for designing a simulator that closely captures real-world conditions. The effectiveness and robustness of both approaches are benchmarked against uncertainties via the built simulator for risky scenarios.

IV. PLATFORM DESCRIPTION

In this section, we describe the fully-actuated aerial vehicle used in this work and the end-effector design for a push-and-slide task on flat surfaces, as in Fig. 1. The fully-actuated aerial vehicle is equipped with tiltable propellers. The baseline interaction control framework of this platform uses a high-level 6-DoF impedance controller and a low-level controller that allocates the 6-DoF wrenches from the high-level controller into propeller rotating speed and the angles of tiltable propeller arms, see Fig. 3. We call the system together with the low-level controller, a state estimator, and an external wrench estimator - the *low-level system*. The state estimator fuses data from the Vicon motion capture system with on-board inertial measurement unit (IMU) measurements. The estimated states are used in an external wrench estimator that follows a momentum-based approach introduced in [22]. With the given control framework the platform can exert forces and torques in all directions at any body orientation, in addition to the gravity compensation. With the body frame $\mathcal{F}_B := \{O_B; \mathbf{x}_B, \mathbf{y}_B, \mathbf{z}_B\}$ attached to its CoM as in Fig. 4a, an end-effector is rigidly attached to the aerial vehicle along the axis \mathbf{z}_B which is defined as the interaction axis. The end-effector is equipped with three omniwheels and the wheels are equally distributed with the same wheel distance $r_d = 0.084$ m from the Center of Geometry (CoG) of the end-effector tip, see Fig 4b. Moreover, they are placed with a 120° angle between each pair to allow sliding motion in an arbitrary direction along a flat surface. Let $h = 0.3$ m be the distance from CoM to end-effector tip along \mathbf{z}_B . A 6-DoF FT (force and torque) sensor is mounted between the end-effector and the aerial vehicle. The sensor frame orientation coincides with the body frame orientation with an offset $h_{ft} = 0.12$ m in axis \mathbf{z}_B between the mounting point of the force sensor and O_B , see Fig. 4a. The FT sensor is used to measure low-level system uncertainties and is not used in the control scheme.

V. FORCE-ANGLE TIP-OVER STABILITY MEASURE

In this section, we present the offline force-angle stability measure from physical experiments with the fully-actuated aerial vehicle in Sec. IV following the methods in [16, 17].

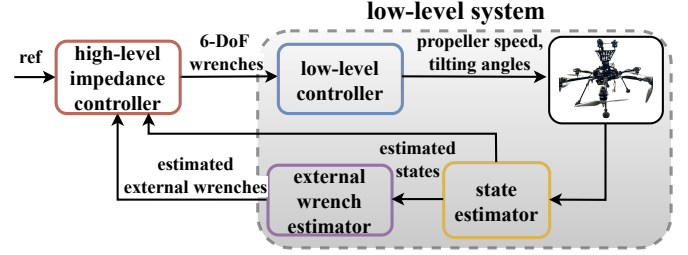


Fig. 3: Baseline interaction control framework of the fully-actuated aerial vehicle.

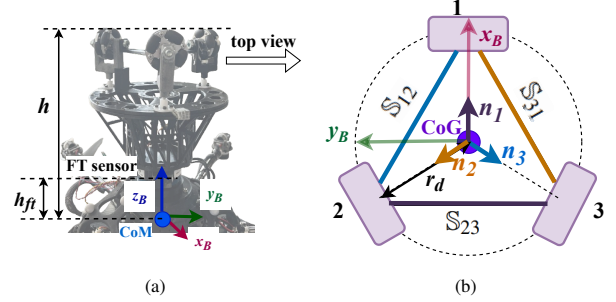


Fig. 4: The (a): end-effector equipped with three omniwheels, body frame at CoM: $\mathcal{F}_B := \{O_B; \mathbf{x}_B, \mathbf{y}_B, \mathbf{z}_B\}$. The (b): top view of the wheel layout, $\mathbf{n}_1, \mathbf{n}_2, \mathbf{n}_3 \in \mathbb{R}^2$ are normal vectors of planes $\mathcal{S}_{23}, \mathcal{S}_{31}$ and \mathcal{S}_{12} introduced in Sec. VI-D.

Furthermore, we derive tip-over avoidance guidelines for hardware design based on the force-angle stability measure.

During the physical experiments, the platform came into contact with a flat surface by pushing toward it and then slid on the surface. While sliding, tip-over instability arises when the robot body undergoes rotation, leading to a decrease in the number of contact points. Eventually, all remaining contact points align along a single line, known as the tip-over axis. For the studied platform with three omniwheels in Fig. 4a, tip-over axes are defined as the lines that join all contact points of the support polygon based on their graphical nature. The force-angle stability measure monitors the tip-over stability using a resultant force vector and a candidate angle about each tip-over axis. This force vector captures the effects of forces and torques acting on the CoM of the system that contribute to the tip-over instability about the corresponding tip-over axis. The candidate angle indicates the tip-over status about the corresponding tip-over axis under the effects of the resultant force vector. The tip-over stability measure of the whole system is thus given by a measure of the most crucial tip-over axis around which the tip-over occurs first.

In the following, we introduce a support pattern associated with the support polygon and its tip-over axes. The support pattern is considered as a stable region within which no tip-over occurs. Furthermore, the resultant force vector definition is presented for the studied system and a candidate angle that presents the tip-over status is defined based on the location of the resultant force vector with respect to (w.r.t.) the support pattern. The resulting data from experiments are used to

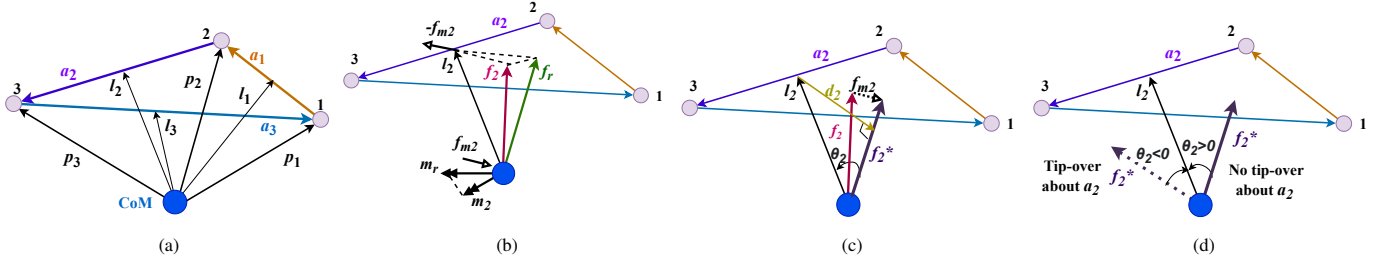


Fig. 5: Force-angle measure definition, (a): support pattern with tip-over axes and their normal vectors; (b): force and torque vectors that participate in tip-over instability; (c): the resultant force vector and the candidate angle; (d) the candidate angle value and corresponding tip-over status.

display the force-angle stability measure of the whole system and derive tip-over avoidance guidelines for hardware design. All vectors in this section are defined in the body frame.

A. The Support Pattern

For a consistent formulation despite the robot body orientation, we define that the wheel number i increases from 1 to 3 following the right-hand rule with the thumb aligning with z_B as in Fig. 5a. The contact points from three wheels form a support polygon on the work surface in the shape of a triangle which introduces three tip-over axes $a_i \in \mathbb{R}^3$, $i = 1, 2, 3$. Let p_i be the position vector of the contact point on wheel i w.r.t. O_B . We define that for $i = 3$, $p_{i+1} := p_1$. Therefore, for $i = 1, 2$, $a_i = p_{i+1} - p_i$, and $a_3 = p_1 - p_3$. We denote $\hat{\cdot}$ as the normalization operator where $\hat{a} = \frac{a}{\|a\|}$ is the unit vector of an arbitrary vector $a \neq 0$. Let l_i be the normal vector of a_i which passes through the CoM and is given by: $l_i = (\mathbb{I}_{3 \times 3} - \hat{a}_i \hat{a}_i^T) p_{i+1}$, where $\mathbb{I}_{3 \times 3}$ is the identity matrix. The support pattern of the studied fully-actuated aerial vehicle is constructed by the defined normal vectors l_i , $i = 1, 2, 3$, and l_i is later used to derive the candidate angle to assess the tip-over status about tip-over axis a_i .

B. The Resultant Force Vector

To find the resultant force vector of the system about each tip-over axis a_i , we first define the forces and torques acting on the system CoM, which participate in tip-over instability via the system's equations of motion. The equations of motion of the system expressed in the body frame are written as:

$$M\dot{v} + Cv + \begin{bmatrix} g^B \\ 0_3 \end{bmatrix} = w_a + w_e, \quad (1)$$

where $v \in \mathbb{R}^6$ is the stacked linear and angular velocity, M and $C \in \mathbb{R}^{6 \times 6}$ are the mass and Coriolis matrices, $g^B \in \mathbb{R}^3$ is the gravity force vector, $w_a = [f_a^T \ \tau_a^T]^T$ and $w_e \in \mathbb{R}^6$ are the actuation wrenches and external wrenches, respectively. We assume that only the contact forces between the end-effector and the work surface contribute to the external wrenches. The contact forces do not participate in tip-over instability [16]. The effects of systematic uncertainties and other possible disturbances (wind gusts etc.) on tip-over stability measures are often addressed by increasing the stability margin [23]. Being different from mobile manipulators that usually have actuated wheels, for passive sliding with aerial vehicles,

the aerial system generates actuation forces to enable the sliding motion and push towards the work surface. Therefore, the forces and torques acting on the aerial system CoM that participate in tip-over instability are defined as:

$$f_r = f_a - g^B, \quad m_r = \tau_a. \quad (2)$$

For a given tip-over axis a_i , only the components of f_r and m_r that act about a_i would contribute to tip-over instability about a_i . As shown in Fig. 5b, the components of f_r and m_r about a_i are given by: $f_i = (\mathbb{I}_{3 \times 3} - \hat{a}_i \hat{a}_i^T) f_r$ and $m_i = (\hat{a}_i \hat{a}_i^T) m_r$. Furthermore, the effects of m_i on tip-over instability about a_i need to be represented in the form of equivalent forces. To do so, we introduce an equivalent force couple, i.e., two force vectors acting on different locations, to replace the torque vector m_i . With infinite possible force locations and directions, a reasonable choice introduced by [16] is to use a force couple $(-f_{mi}, f_{mi})$, where $-f_{mi}$ passes through the cross point of a_i and l_i , and f_{mi} passes through O_B , see Fig. 5b. The member of the force couple acting at the CoM is given by: $f_{mi} = \frac{l_i \times m_i}{\|l_i\|}$. Finally, as shown in Fig. 5c, the resultant force vector about tip-over axis a_i that captures both effects of forces and torques is given by:

$$f_i^* = f_i + f_{mi}. \quad (3)$$

C. Stability Measure of the Fully-Actuated Aerial Vehicle

With the defined normal vector l_i and the resultant force vector f_i^* about each axis a_i and their unit vectors \hat{l}_i, \hat{f}_i^* , the previously mentioned candidate angle used for stability measure is defined as $\theta_i = \sigma_i \cos^{-1}(\hat{f}_i^* \cdot \hat{l}_i) \in [-\pi, \pi]$, see Fig. 5d. σ_i is the sign of θ_i , which signals if the force vector f_i^* is inside the support pattern, and is given by:

$$\sigma_i = \begin{cases} +1 & (\hat{f}_i^* \times \hat{l}_i) \cdot \hat{a}_i > 0, \\ -1 & \text{otherwise.} \end{cases} \quad (4)$$

When the angle has a positive sign, it indicates that the force vector f_i^* is inside the support pattern, and tip-over about axis a_i is in progress if the sign is negative. The critical case is $\theta_i = 0$ when f_i^* coincides with l_i . Among all the angles θ_i for $i = 1, 2, 3$, the smallest θ_i indicates the most crucial tip-over axis around which the tip-over occurs first. The force-angle stability measure of the whole system is therefore given by:

$$\alpha = \min_{i \in \{1, 2, 3\}} (\theta_i \cdot \|d_i\| \cdot \|f_i^*\|), \quad (5)$$

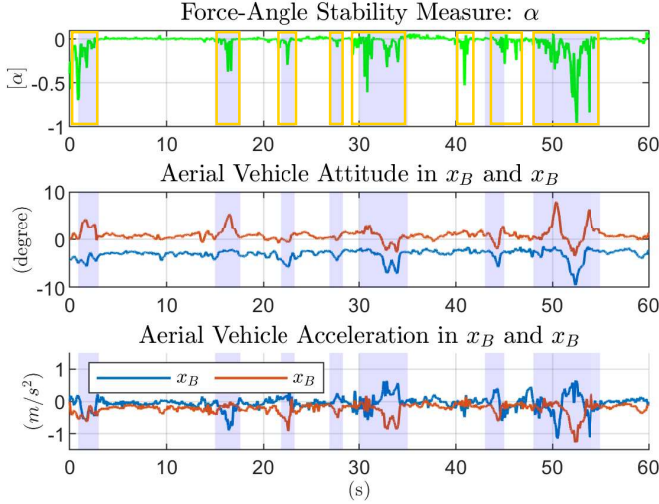


Fig. 6: From top to bottom: force-angle stability measure, aerial vehicle attitude along x_B and y_B , aerial vehicle acceleration along x_B and y_B ; shaded area: visually captured tip-over incidents from the experiment associated with changes of the aerial vehicle attitude in x_B and y_B ; yellow rectangles: expected tip-overs based on the force-angle stability measure.

with $d_i = -I_i + (I_i^\top \cdot \hat{f}_i^*)\hat{f}_i^*$ being the minimum length vector from the tip-over axis a_i to \hat{f}_i^* (for details, please refer to [17]) as in Fig. 5c.

From physical experiments, control wrenches w_a in (1) generated by the propulsion system of the platform, system linear acceleration, and aerial vehicle attitude can be obtained from the low-level system in Fig. 3. With (2) and (5), the force-angle stability measure for the fully-actuated aerial vehicle during passive sliding is displayed in Fig. 6 along with the aerial vehicle attitude and linear acceleration in x_B and y_B . The attitude and linear motion in z_B do not contribute to tip-over. The yellow rectangles in the top plot of Fig. 6 indicate expected tip-overs based on the force-angle stability measure criterion, while the shaded area presents visually captured tip-over incidents from the experiment. During the experiment, tip-overs were associated with evident changes in aerial vehicle orientation along x_B and y_B , as shown in the middle plot of Fig. 6. The force-angle stability measure effectively captures most of the tip-over incidents during the experiments, proving its reliability in assessing potential instances of robot tip-over instability. The uncertainties from the low-level system can affect the accuracy of the tip-over prediction, which makes the force-angle stability measure less robust to be used in real-time tip-over control, but an efficient tool to evaluate the likelihood of tip-over instability with the system setup.

Tip-overs generally occurred when there was an explicit increase of the sliding acceleration (i.e., the linear acceleration along x_B and y_B) magnitude. In regions where no tip-over is detected by the force-angle stability criterion, the measured stability has very small values, being slightly above the critical case when $\alpha = 0$. Being too close to the critical case heightens the system's sensitivity to the effects of systematic

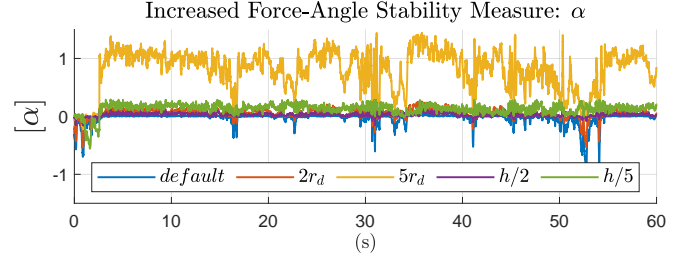


Fig. 7: Increased stability measure by increasing r_d to $2r_d$, $5r_d$ with constant h , and reducing h to $h/2$, $h/5$ with constant r_d .

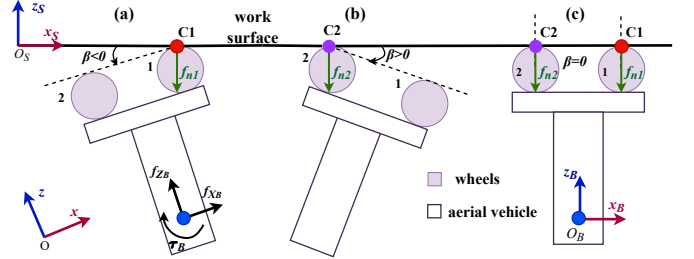


Fig. 8: Planar two-wheeled system and coordinate frames, (a): tip-over with $\beta < 0$, wheel 1 in contact; (b): tip-over with $\beta > 0$, wheel 2 in contact; (c): full-contact with $\beta = 0$.

uncertainties or disturbances. As a result, the likelihood of tip-over instability increases when subjected to these effects. Hence, to prevent tip-overs in the presence of uncertainties and potential disturbances, it is essential to increase the system's stability measure effectively. This entails establishing a substantial margin between the stability measure value and the critical value.

D. Guidelines for Tip-over Avoidance

In this section, we present tip-over avoidance guidelines that aid in increasing the tip-over stability and avoiding the critical case. Based on the definition in Sec. V-C, the key to avoiding tip-overs is to keep the force vector \hat{f}_i^* inside the support pattern. This can be achieved by either limiting the force vector direction or enlarging the support pattern. During passive sliding, the fully-actuated aerial vehicle has to exert a pushing force along the interaction axis z_B while supplying also the lateral forces along x_B and y_B to enable sliding motion. Hence, as the sliding acceleration magnitude rises, the lateral forces also increase, resulting in a simultaneous decrease in the stability measure as shown in Fig. 6. Either reducing the sliding acceleration or increasing the pushing force magnitude can enhance stability without changing the support pattern. Nevertheless, this approach imposes constraints on the application range, demands varied sliding accelerations and entails increased energy consumption when generating higher pushing forces. Consequently, we focus on hardware guidelines to enlarge the support pattern. This can be achieved by either increasing the support polygon (i.e., rising r_d) or reducing the distance from the CoM to the end-effector tip (i.e., decreasing h). With the same acceleration and force data used in Fig. 6, we increase r_d to $2r_d$, $5r_d$, and reduce h to $h/2$,

$h/5$. The effectiveness of increasing the stability measure by enlarging the support pattern is shown in Fig. 7. Notably, even scaling up r_d or scaling down h twice does not significantly improve the stability measure. In practical terms, doubling the end-effector tip size results in a bulky design relative to the aerial vehicle size and mass. Additionally, there is a lower limit for h to safeguard the propellers from contacting the work surface.

The guidelines based on the force-angle stability measure can help us prevent tip-overs during sliding via hardware design and avoid investigation in control design. However, misalignment between the end-effector tip and the work surface at initial contact remains unresolved with the baseline impedance control. Moreover, Fig. 7 shows even with $2r_d$, $h/2$, or $h/5$, the stability measure still approaches the critical value 0 or even negative value for riskier scenarios when sliding maneuvers occur. To address the tip-over issue during both initial contact and sliding in risky scenarios, we introduce a control strategy for tip-over recovery from misalignment at initial contact and tip-over avoidance during sliding in the next section. In the control design, the normal-force-based tip-over stability criterion is used, which explicitly and accurately measures the tip-over instability despite the systematic uncertainties.

VI. CONTROL FOR TIP-OVER RECOVERY AND AVOIDANCE

In this section, we present a high-level control strategy to improve the 6-DoF impedance controller in Fig. 3 which resolves the tip-over issue during both initial contact and sliding on an unknown flat surface, even under risky scenarios. The normal-force-based tip-over stability criterion [11] is used in designing the controller considering that normal forces acting on wheels can be measured by attaching pressure sensors. From the definition of multi-wheeled systems, two wheels are the minimum number of wheels in a multi-wheeled locomotion problem. Hence, the two-wheeled system is fundamental for studying the tip-over problem [16]. Without affecting the main contribution, we introduce the tip-over stability criterion and interaction control framework of a fundamental planar two-wheeled system. Later, we present the method to extend the control design from the planar system to a three-wheeled system as Fig. 1 in 3D (dimensional) space.

A. Planar Two-Wheeled System

To capture the main characteristics of passive sliding with the studied fully-actuated aerial vehicle on a flat work surface, we present a simplified two-wheeled system model in a 2D plane. The force and torque generation ability of the platform in Sec. IV allows us to neglect gravity force in the simplified system, and with the focus on high-level control design, we assume that the system can directly supply actuation forces in any direction of the 2D plane and the actuation torque along the axis perpendicular to the plane. Now consider a two-wheeled system as in Fig. 8, in which wheel 1 and wheel 2 have their centers rigidly connected to an aerial vehicle which is assumed to be a rigid body. Two wheels can freely rotate

TABLE I: Notation

i	wheel number
C_i	the contact point on wheel i
m_B	the total mass of the system
<u>Coordinate frames:</u>	
\mathcal{F}_w'	the world frame of any motion, $\mathcal{F}_w' := \{O; \mathbf{x}, \mathbf{z}\}$
\mathcal{F}_S'	the work frame attached to the work surface, $\mathcal{F}_S' := \{O_S; \mathbf{x}_S, \mathbf{z}_S\}$
\mathcal{F}_B'	the body frame attached to the CoM of the system, $\mathcal{F}_B' := \{O_B; \mathbf{x}_B, \mathbf{z}_B\}$
<u>State variables:</u>	
x	the position of CoM w.r.t. O along \mathbf{x}_B
β	the orientation of the body frame w.r.t. the work frame being positive clockwise, $\beta < 0$ when only wheel 1 is in contact, $\beta > 0$ when only wheel 2 is in contact, and $\beta = 0$ for full-contact, see Fig. 8
<u>Contact forces:</u>	
f_{ni}	the normal force acting on wheel i , $f_{ni} \geq 0$
<u>Actuation wrenches:</u>	
f_{X_B}	actuation force acting on CoM along \mathbf{x}_B , $f_{X_B} \in \mathbb{R}$
f_{Z_B}	actuation force acting on CoM along \mathbf{z}_B , $f_{Z_B} \in \mathbb{R}$
\mathbf{f}_B	the actuation linear force vector expressed in body frame, $\mathbf{f}_B = [f_{X_B} \ f_{Z_B}]^\top \in \mathbb{R}^2$
τ_B	the actuation rotational torque along the axis perpendicular to the 2D plane, being positive clockwise, $\tau_B \in \mathbb{R}$

TABLE II: Contact Conditions

Contact Condition	f_{n1}	f_{n2}	β	Control Objective
free flight	$< \delta_F$	$< \delta_F$	-2	full-pose control
tip-over	$\geq \delta_F$	$< \delta_F$	-1	tip-over recovery
tip-over	$< \delta_F$	$\geq \delta_F$	+1	tip-over recovery
full-contact	$\geq \delta_F$	$\geq \delta_F$	0	tip-over avoidance

around the axis perpendicular to the 2D plane. When both wheels are in contact with the work surface, we define such contact condition as *full-contact*. On the other hand, when there is only one wheel in contact, it is referred to as a tip-over. The notations used in the following sections are displayed in Table I. Without including uncertainties and other external disturbances apart from the contact wrenches in the system modeling, the system's equations of motion expressed in the body frame are given by:

$$\mathbf{M}_S \dot{\mathbf{v}}_S + \mathbf{C}_S \mathbf{v}_S = \mathbf{w}_B + \mathbf{w}_C, \quad (6)$$

where $\mathbf{v}_S \in \mathbb{R}^3$ is the stacked linear and angular velocity, \mathbf{M}_S and $\mathbf{C}_S \in \mathbb{R}^{3 \times 3}$ are the mass and Coriolis matrices, $\mathbf{w}_B = [\mathbf{f}_B^\top \ \tau_B]^\top$ and $\mathbf{w}_C \in \mathbb{R}^3$ are the actuation wrenches and contact wrenches respectively. As shown in Fig. 8, a tip-over with $\beta < 0$ indicates when only wheel 1 is in contact, a tip-over with $\beta > 0$ indicates when only wheel 2 is in contact, and $\beta = 0$ indicates when the system is in full-contact. During tip-overs, the system is only subjected to the contact forces acting on one contact point C_i depending on which wheel is in contact. In full-contact, the contact forces act on both wheels.

B. Normal-Force-based Tip-Over Stability Criterion

In this section, we present the normal-force-based tip-over stability criterion for the modeled two-wheeled system. The normal forces acting on wheels are used to identify the contact

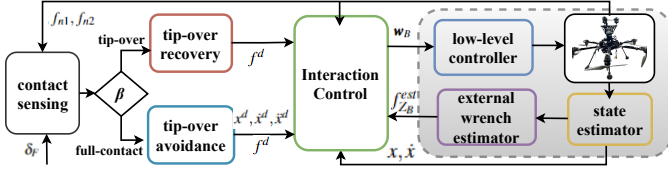


Fig. 9: Interaction control framework for tip-over recovery and avoidance.

conditions between the system and the work surface. When the normal force on a wheel goes to zero, it means this wheel is detached from the work surface. To increase the robustness of tip-over detection, instead of zero, we use a positive margin δ_F . With δ_F , we define four contact conditions, as shown in Table II. We set $\beta = -2$ for free flight, $\beta = 0$ for full-contact, $\beta = -1$ when wheel 1 is in contact during the tip-over, and $\beta = +1$ when wheel 2 is in contact during the tip-over, such that the contact conditions are discretized and can be used in the control design. This process is then realized in the control framework using a pressure sensor below each wheel that provides contact sensing. Only if full-contact or a tip-over condition is detected, the interaction controller is enabled. When the system is resting in full-contact without sliding by only pushing towards the surface along the interaction axis (i.e., the static contact), ideally the normal forces acting on two wheels are equal without considering uncertainties and other potential disturbances due to symmetric properties [11]. When the system tends to tip over, the normal force on one wheel starts to reduce while the difference between the normal forces on two wheels increases. Therefore, we define the static contact case as the nominal contact, where:

$$f_{n1} = f_{n2}, \text{ with } f_{n1}, f_{n2} \geq \delta_F. \quad (7)$$

The tip-over stability criterion is used to monitor the contact conditions. We use the nominal contact case to derive the control law in the following section. The (7) is however only a sufficient condition of full-contact while having both $f_{n1}, f_{n2} \geq \delta_F$ is considered as a necessary condition of full-contact.

C. Interaction Control Framework

In this section, we present the high-level interaction control framework for push-and-slide tasks. A block diagram of the proposed system is shown in Fig. 9. The controller is formulated in body frame \mathcal{F}'_B , as uncertainties about surface location and orientation render a world frame formulation impractical. When the system is in a tip-over, sending sliding motion references (i.e., linear acceleration, velocity, and position references along x_B) that are not in parallel with the flat surface often leads to instability. Therefore, when a tip-over is in progress, we set the sliding motion references to zeros until the system gains full-contact. Based on the identified contact conditions in Table II, we introduce two control objectives by monitoring the tip-over status. When the system is in a tip-over, the control objective is to recover from the tip-over. When the system is in full-contact, the control objective is to avoid tip-overs

while following sliding motion references along the surface. The designed controller provides high-level control outputs described as the actuation wrench w_B in the body frame, fed to the low-level system for actuation allocation.

With the defined control objectives, we propose a hybrid motion/force control approach, which we call the *normal-force control*. In the normal-force control scheme, the pushing force along axis z_B and the linear motion along axis x_B are feedback controlled with force estimation and state estimation from the low-level system. The rotational torque of the 2D plane (being positive clockwise) is controlled using the normal forces measured on both wheels. The direct force control along z_B allows the system to exert a specific force on the work surface, and also to ensure physical contact between the system and the work surface. The linear motion control along x_B tracks the sliding motion trajectory according to task-specific requirements. Finally, the torque control handles the tip-over problem. We denote $x^d, \dot{x}^d, \ddot{x}^d$ as sliding motion references along x_B , and f^d as the force reference along z_B . We define the linear motion and force tracking errors expressed in the body frame as $e_p = x - x^d$, $e_d = \dot{x} - \dot{x}^d$, and $e_f = f_{Z_B}^{est} - f^d$, where $f_{Z_B}^{est}$ is the estimated force along z_B from the external wrench estimator.

Considering the tip-over stability criterion described in the last section, and aiming at achieving the full-contact described in Table II, we consider the nominal contact case in (7) as the reference condition of the control design. We define the force difference error between the normal force measurements on two wheels as:

$$e_n = f_{n1} - f_{n2}. \quad (8)$$

Since $e_n = 0$ is not necessary for having full-contact, a range of force difference error e_n can be acceptable while achieving full-contact. This property naturally leads to a proportional control design. With acceptable force difference errors, the system saves energy while preserving the full-contact between the end-effector tip and the work surface during interactions. With a proportional controller, the nominal contact condition thus serves as a guiding condition to let the system rotate in the desired direction towards full-contact. We denote $w_n = [f_x \ f_z \ \tau_1]^T \in \mathbb{R}^3$ as the control wrenches along x_B , y_B and the rotation axis. With the above definitions, the control wrenches are given by:

$$f_x = m_B \ddot{x}^d - k_p e_p - k_d e_d, \quad (9a)$$

$$f_z = f^d - k_f e_f - k_I \int e_f, \quad (9b)$$

$$\tau_1 = k_n e_n, \quad (9c)$$

where k_p, k_d, k_f, k_I, k_n are positive gains. The final actuation wrenches w_B is defined as: $w_B = w_n + C_S v_S$. With (6), the closed loop dynamics of the system yield:

$$M_S \dot{v}_S = w_n + w_C. \quad (10)$$

TABLE III: Plane Definition

Plane	Left wheel	Right wheel	Normal vector	Tracking error
\mathbb{S}_{23}	2	3	\mathbf{n}_1	e_{n1}
\mathbb{S}_{31}	3	1	\mathbf{n}_2	e_{n2}
\mathbb{S}_{12}	1	2	\mathbf{n}_3	e_{n3}

D. Three-Wheeled System

In the previous section, we presented the normal-force control design for a simplified planar two-wheeled system, to illustrate how we solve the tip-over issue. In this section, we extend the method from a two-wheeled planar system to the full three-wheeled system shown in Fig. 4a, with a focus on torque control. For the three-wheeled system with six DoFs, similar to the hybrid motion/force control in Sec. VI-C, the force along \mathbf{z}_B and the linear motion along \mathbf{x}_B and \mathbf{y}_B are feedback controlled. The torque control related to the angular dynamics of the system however needs further investigation, since there are two more DoFs compared to the planar case. We define the torque control wrench along \mathbf{x}_B and \mathbf{y}_B used for tip-over recovery and avoidance as $\boldsymbol{\tau}_2 \in \mathbb{R}^2$. The platform orientation along \mathbf{z}_B does not contribute to the tip-over behavior, therefore the control wrench along \mathbf{z}_B is obtained via attitude control. The three wheels form a support polygon with three sides as in Fig. 4b. Each side of the support polygon is defined by two contact points which can be interpreted as a two-wheeled planar system. Each plane of the interpreted planar system from all three sides of the support polygon is defined in Table III. The torque control wrench $\boldsymbol{\tau}_2$ is thus the sum of the torque control wrench of each plane in 3D space. To combine the torque control wrench of each plane in body frame, we define three unit vectors $\mathbf{n}_1, \mathbf{n}_2, \mathbf{n}_3 \in \mathbb{R}^3$ parallel to the plane $(\mathbf{x}_B, \mathbf{y}_B)$ indicating the positive direction of the rotation and torque in planes $\mathbb{S}_{23}, \mathbb{S}_{31}$ and \mathbb{S}_{12} , respectively, see Fig. 4b. Knowing the force measurements on three wheels f_{n1}, f_{n2} and f_{n3} respectively, based on the tip-over stability criterion in Sec. VI-B, the full-contact scenario of the three-wheeled system is defined by: $f_{ni} \geq \delta_F$, with $i = 1, 2, 3$. Similarly, the nominal contact case is given by:

$$f_{n1} = f_{n2} = f_{n3}. \quad (11)$$

The corresponding force difference errors of each plane are defined as $e_{n1} = f_{n3} - f_{n2}$, $e_{n2} = f_{n1} - f_{n3}$, and $e_{n3} = f_{n2} - f_{n1}$. The torque control wrench $\boldsymbol{\tau}_2$ is given by:

$$\boldsymbol{\tau}_2 = k_{n1}e_{n1}\mathbf{n}_1 + k_{n2}e_{n2}\mathbf{n}_2 + k_{n3}e_{n3}\mathbf{n}_3, \quad (12)$$

where k_{n1}, k_{n2}, k_{n3} are positive gains. This methodology can also be applied to four-wheeled systems or other multi-wheeled layouts.

VII. VALIDATION

In this section, we present the validation of the control design in Sec. VI-C and benchmark the tip-over avoidance guidelines in Sec. V-D under realistic systematic uncertainties. To test the robustness of the proposed approaches in risky

scenarios, e.g., sliding maneuvers, we use simulations to avoid hazardous operations of the real platform. Moreover, to take into account the uncertainties from the real low-level system, we identify the force and torque uncertainties at the CoM of the system using FT sensor measurements from physical experiments. Later, a simulator based on the system in Fig. 8 is built to simulate the tip-over problem for passive sliding with fully-actuated aerial vehicles. We calibrate the simulator based on the experimentally determined uncertainties in force-torque application and end-effector pressure sensing. The measured uncertainties take into account the modeling errors from force estimation, state estimation, low-level control, and sensor noises.

The system performance is evaluated by the force difference error e_n (8) from contact points and the contact condition β in Table II based on Sec. VI-B. In total, four scenarios are tested for tip-over avoidance, involving different sliding accelerations and pushing force magnitudes. As a baseline, we compare against the simulation results using impedance control with the same wheel distance $r_d = 0.084$ m as the real platform, which reflects the physical experiments in Sec. V. Following the guidelines in Sec. V-D, a reasonable hardware design to avoid tip-over considering the platform size is to have twice the wheel distance as $2r_d$, based on the results in Fig. 7. Two approaches including using an enlarged end-effector ($2r_d$) with the baseline impedance control and an implementation of the control design in Sec. VI are tested and compared. In a high-risk scenario, we evaluate the impact of variable contact angles (i.e., the relative angles between the surface and the end-effector tip) to validate the robustness of the normal-force controller in tip-over recovery. The control design in Sec. VI-D for a three-wheeled system is also validated with a simulator calibrated with measured uncertainties and modeled pressure sensor noises in high-risk scenarios.

A. Uncertainty Identification

In physical experiments, we used the FT sensor shown in Fig. 4a to measure the external forces $\mathbf{F}_{meas} \in \mathbb{R}^3$ and torques $\boldsymbol{\tau}_{meas} \in \mathbb{R}^3$ acting on the mounting point of the sensor in body frame when the system is in contact. We denote $\mathbf{p}_{ft} \in \mathbb{R}^3$ as the position vector from the mounting point of the FT sensor to the CoM of the system expressed in the body frame. With the parameters in Sec. IV, we have $\mathbf{p}_{ft} = [0 \ 0 \ -h_{ft}]^\top$ for the hardware setup. During the experiments, the desired pushing force along \mathbf{z}_B was 10 N. With the rigid body assumption, the linear forces acting on the CoM of the system are equal to \mathbf{F}_{meas} . The torques acting on the CoM are calculated via a simple transformation: $\boldsymbol{\tau}_{meas}^{CoM} = \boldsymbol{\tau}_{meas} + \mathbf{F}_{meas} \times \mathbf{p}_{ft}$. From the model-based force estimation in the low-level system, we obtain the estimated external forces and torques at the CoM as \mathbf{F}_{est} and $\boldsymbol{\tau}_{est}$ expressed in body frame. With the above information, we identify systematic uncertainties in the form of force and torque generation expressed in body frame by: $\mathbf{F}_{unc} = \mathbf{F}_{meas} - \mathbf{F}_{est}$, and $\boldsymbol{\tau}_{unc} = \boldsymbol{\tau}_{meas}^{CoM} - \boldsymbol{\tau}_{est}$. The experimentally obtained force and torque uncertainties at the CoM are displayed in Fig. 10. The results show that there

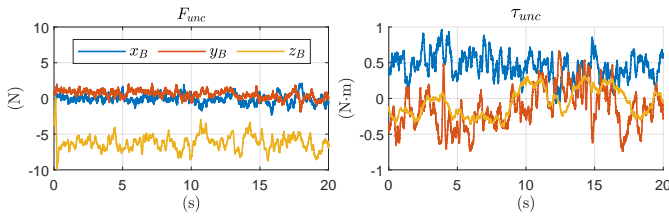


Fig. 10: Measured force and torque uncertainties at the CoM of the system from the low-level system expressed in body frame.

are significant modeling errors in force estimation since the force error magnitude along axis z_B is almost the same as the desired force value. The uncertainties in angular dynamics τ_{unc} hint at CoM offsets, which are crucial in push-and-slide tasks. The identified uncertainties are later integrated with the actuation wrenches from the high-level controller in the simulator.

B. Simulator Setup

A Simscape model based on the system described in Fig. 8 is used for testing. The proposed controller in Sec. VI-C and the baseline controller are implemented via Matlab/Simulink at 100Hz. The Simscape model captures the main geometric parameters of the real platform, i.e., the wheel radius and wheel distance. The friction coefficients at contact are set to have similar values to the real experiment setup during passive sliding tasks. In the simulation, we command the system to approach a flat work surface with different contact angles $\delta\beta$ to simulate the tip-over at initial contact with an unknown surface. Once the system gains full-contact, it will slide along the work surface with a desired maximum acceleration $a_{max} = 0.5 \text{ m s}^{-2}$. To capture the effects of uncertainties with higher magnitude, the identified force uncertainties along x_B and z_B , and the identified torque uncertainties along axis x_B are integrated with f_{x_B} , f_{z_B} and τ_B from the high-level controller, respectively. The data in Fig. 10 is resampled according to the simulation sample time to be simultaneous with the actuation wrenches in the simulator. The simulated actuation wrenches are given by: $f_{x_B}^{sim} = f_{x_B} - [1 \ 0 \ 0] \mathbf{F}_{unc}$, $f_{z_B}^{sim} = f_{z_B} - [0 \ 0 \ 1] \mathbf{F}_{unc}$, $\tau_B^{sim} = \tau_B - [1 \ 0 \ 0] \boldsymbol{\tau}_{unc}$. Moreover, the pressure sensor noises are simulated via a Gaussian distribution with a scale of 10 percentage of the data magnitude, which is a choice based on preliminary tests with pressure sensors. With the simulator setup, we can test the controller behavior for both tip-over recovery and avoidance in the presence of uncertainties. We apply a similar approach to include the measured uncertainties in the tests using the baseline impedance controller.

The control gains related to motion and force control used in (9a) and (9b) are selected according to the baseline impedance controller used in the previous work. For the gain k_n used in the normal-force-based torque control in (9c), a heuristic tuning method was applied. An initial guess was based on the ratio between the magnitude of the system's maximum applicable torque within saturation and the desired pushing force f^d . Then we adjusted the initial gain value

TABLE IV: Testing Scenarios

Case Number	maximum sliding acc (m s^{-2})	pushing force (N)
(a)	$ a_{max} $	$ f_{z_B}^{sim} $
(b)	$5 a_{max} $	$ f_{z_B}^{sim} $
(c)	$ a_{max} $	$0.5 f_{z_B}^{sim} $
(d)	$5 a_{max} $	$0.5 f_{z_B}^{sim} $

until the system gave a robust tip-over recovery and avoidance behavior even in the presence of the measured uncertainties. For simulating the actuator saturation of the physical platform, the upper and lower limits of the controlled torque are set to $\pm 5 \text{ N m}$ in the simulations, with $k_n = 0.5$.

C. Robustness Test for Tip-Over Avoidance

In this section, we present the robustness tests using differently scaled maximum sliding acceleration $|a_{max}| = 0.5 \text{ m s}^{-2}$ and pushing force $|f_{z_B}^{sim}| \approx 15 \text{ N}$ for tip-over avoidance during sliding assuming that the initial alignment is achieved. To do so, four scenarios with the simulation setup in the last section are tested as shown in Table. IV. Based on the analysis in Sec. V, the testing scenario is riskier when larger sliding accelerations or smaller pushing forces are used. Therefore (d) is the most critical testing scenario among the four. As a comparison, the baseline impedance controller, the enlarged end-effector with impedance control, and the control scheme in Sec. VI-C are tested in all four scenarios. The resulting force difference error e_n and the contact condition β are shown in Fig. 11 and Fig. 12 respectively. Fig. 12 indicates that tip-overs occurred for all testing scenarios when the baseline impedance control was applied. The e_n resulting from using the impedance controller under scenario (d) is not shown in Fig. 11 (d) because instability occurred at initial contact. In Fig. 12, the enlarged end-effector did avoid tip-over for the first two scenarios (a) and (b), however tip-over happened in riskier scenarios (c) and (d) when the pushing force is smaller. The normal-force controller instead effectively avoided tip-over for all four scenarios including sliding maneuvers and a smaller pushing force with very small errors e_n as in Fig. 11. Even in scenario (a) and (b) in Fig. 11, when tip-over was avoided by both enlarging the end-effector and the normal-force control, the error e_n from the normal-force control has a much smaller magnitude and oscillation compared to the one from the enlarged end-effector. From these results, we see that the enlargement of the end-effector is an effective approach to alleviate the impact of contact uncertainties on the system during sliding in low-risk scenarios. However, the proposed normal-force control approach is effective and robust even in high-risk scenarios.

D. Robustness Test for Tip-Over Recovery

In this section, we validate the robustness of the designed controller for tip-over recovery from initial misalignment under the most critical scenario from the last section: scenario (d) with $5|a_{max}|$ and $0.5|f_{z_B}^{sim}|$. We let the system approach the work surface with a contact angle $\delta\beta$. With $\delta\beta = 0$,

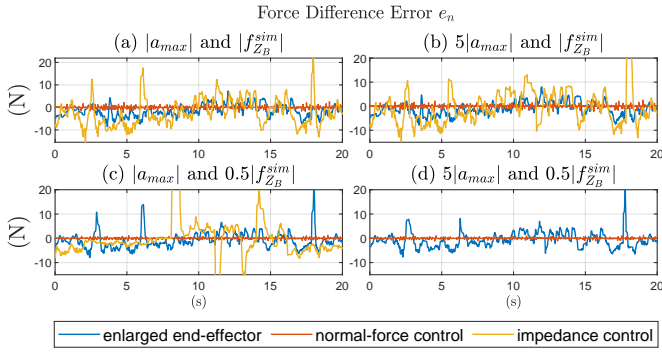


Fig. 11: Force difference error e_n for differently scaled $|a_{max}|$ and $|f_{Z_B}^{sim}|$ benchmarking the impedance control, enlarged support polygon with impedance control, and the normal-force control. In (d) no data is displayed for the impedance control case due to instability at initial contact.

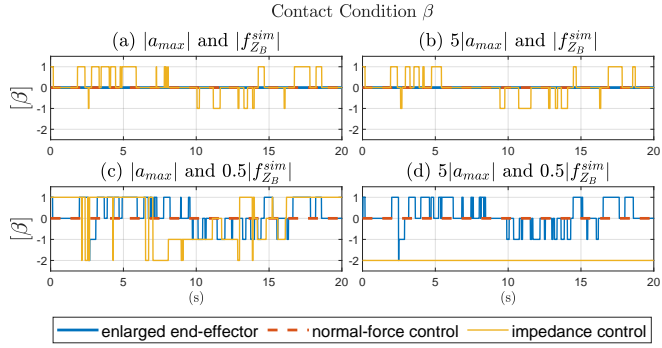


Fig. 12: Contact conditions: for impedance control tip-overs occurred in all scenarios, for enlarged end-effector tip-overs occurred in (c) and (d), and for normal-force control, no tip-overs occurred in all scenarios. In (d) instability happened for the impedance control case at initial contact, and β is presented by -2 same as the value for free flight.

we can simulate the possible misalignment due to systematic uncertainties. With $\delta\beta \neq 0$, we can simulate the case when the system approaches an unknown surface with a wrong attitude reference e.g., due to uncertainties in estimating the surface normal, where initial tip-over occurs. The tip-over recovery operation is tested for $\delta\beta = 0^\circ, 10^\circ, 20^\circ$, with the later ones being very critical cases in reality. The resulting force difference error e_n is shown in Fig. 13 (I), in which the high peak values indicate the initial impact when the wheel contacts the surface, which is quite high for larger contact angles. The system can recover from the initial tip-over for all three cases. From the results, we conclude that the normal-force control can robustly recover from tip-over situations.

E. Three-Wheeled System

Finally, a similar simulation setup is used for a three-wheeled system as in Fig. 4a. The identified uncertainties in all six directions in Fig. 10 are integrated with the actuation wrenches. To validate the extended control design in Sec. VI-D, we let the system approach the surface with different orientations in \mathbf{x}_B and \mathbf{y}_B with $5|a_{max}|$ and $0.5|f_{Z_B}^{sim}|$. An example of approaching the surface with angle derivation w.r.t. the surface as -5° in \mathbf{y}_B and 15° in \mathbf{x}_B is shown in

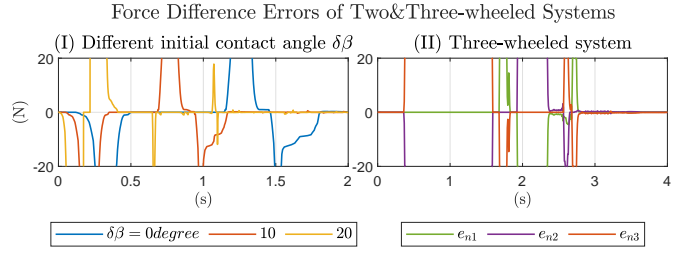


Fig. 13: Tip-over recovery and avoidance with normal-force control under $5|a_{max}|$ and $0.5|f_{Z_B}^{sim}|$ for (I): different initial contact angle $\delta\beta = 0^\circ, 10^\circ, 20^\circ$ of the planar system; (II): contact angle -5° in \mathbf{y}_B and 15° in \mathbf{x}_B of the three-wheeled system.

Fig. 13 (II), where the force difference errors e_{n1} , e_{n2} and e_{n3} of three planes all converge to the equilibrium state. The system can gain full-contact of three wheels with the surface and avoid tip-overs in risky scenarios. With the results, we demonstrated the use case of the normal-force control design for three-wheeled systems applying the proposed method in Sec. VI-D, which promises the generality of such a control strategy.

VIII. CONCLUSION

In this work, we presented a detailed study of multi-wheeled locomotion with fully-actuated aerial vehicles. By careful examination of the tip-over problem in push-and-slide tasks on unknown flat surfaces, we identified common challenges that arise when using standard full-pose controllers for such tasks. We propose two approaches to address the tip-over issue, one involving hardware design guidelines, and one via interaction control design. Both approaches are validated and evaluated using a realistic simulator that is grounded in experimental data and the corresponding realistic uncertainties. Through our analysis, we identified promising avenues for future work, such as the inclusion of simple pressure-based contact sensing at the end-effector, and control systems that make use of them.

IX. ACKNOWLEDGEMENT

This work has been supported by the European Unions Horizon 2020 Research and Innovation Programme AERO-TRAIN under Grant Agreement No. 953454.

REFERENCES

- [1] S. Ali A. Moosavian and Khalil Alipour. Moment-Height Tip-Over Measure for Stability Analysis of Mobile Robotic Systems. In *2006 IEEE/RSJ International Conference on Intelligent Robots and Systems*, pages 5546–5551, 2006. doi: 10.1109/IROS.2006.282270.
- [2] Karen Bodie, Maximilian Brunner, Michael Pantic, Stefan Walser, Patrick Pfandler, Ueli Angst, Roland Siegwart, and Juan Nieto. An Omnidirectional Aerial Manipulation Platform for Contact-Based Inspection. In *Robotics: Science and Systems*, 2019. doi: <https://www.roboticsproceedings.org/rss15/p19.pdf>.

- [3] Xiaojun Ding, Yi Liu, Jin Hou, and Qin Ma. Online Dynamic Tip-Over Avoidance for a Wheeled Mobile Manipulator With an Improved Tip-Over Moment Stability Criterion. *IEEE Access*, 7:67632–67645, 2019. doi: 10.1109/ACCESS.2019.2915115.
- [4] A. Ghasempoor and N. Sepehri. A measure of machine stability for moving base manipulators. In *Proceedings of 1995 IEEE International Conference on Robotics and Automation*, volume 3, pages 2249–2254 vol.3, 1995. doi: 10.1109/ROBOT.1995.525596.
- [5] Q. Huang, S. Sugano, and I. Kato. Stability control for a mobile manipulator using a potential method. In *Proceedings of IEEE/RSJ International Conference on Intelligent Robots and Systems (IROS'94)*, volume 2, pages 839–846 vol.2, 1994. doi: 10.1109/IROS.1994.407542.
- [6] Tong Hui, Florian Braun, Nicolas Scheidt, Marius Fehr, and Matteo Fumagalli. Versatile Airborne Ultrasonic NDT Technologies via Active Omni-Sliding with Over-Actuated Aerial Vehicles. In *Proceedings of 18th International Symposium on Experimental Robotics*, 2023. doi: <https://doi.org/10.48550/arXiv.2311.04662>.
- [7] Guangying Jiang, Richard Voyles, Kenneth Sebesta, and Helen Greiner. Estimation and optimization of fully-actuated multirotor platform with nonparallel actuation mechanism. In *2017 IEEE/RSJ International Conference on Intelligent Robots and Systems (IROS)*, pages 6843–6848, 2017. doi: 10.1109/IROS.2017.8206605.
- [8] Mina Kamel, Sebastian Verling, Omar Elkhatab, Christian Sprecher, Paula Wulkop, Zachary Taylor, Roland Siegwart, and Igor Gilitschenski. The Voliro Omnidirectional Hexacopter: An Agile and Maneuverable Tilttable-Rotor Aerial Vehicle. *IEEE Robotics & Automation Magazine*, 25(4):34–44, 2018. doi: 10.1109/MRA.2018.2866758.
- [9] Evan Kaufman, Kiren Caldwell, Daewon Lee, and Taeyoung Lee. Design and development of a free-floating hexrotor UAV for 6-DOF maneuvers. In *2014 IEEE Aerospace Conference*, pages 1–10, 2014. doi: 10.1109/AERO.2014.6836427.
- [10] Christian Lanegger, Marco Ruggia, Marco Tognon, Lionel Ott, and Roland Siegwart. Aerial Layouting: Design and Control of a Compliant and Actuated End-Effector for Precise In-flight Marking on Ceilings. In *Robotics: Science and Systems*, 2022. doi: <https://www.roboticsproceedings.org/rss18/p073.pdf>.
- [11] Yugang Liu and Guangjun Liu. Interaction Analysis and Online Tip-Over Avoidance for a Reconfigurable Tracked Mobile Modular Manipulator Negotiating Slopes. *IEEE/ASME Transactions on Mechatronics*, 15(4):623–635, 2010. doi: 10.1109/TMECH.2009.2031174.
- [12] Grzegorz Malczyk, Maximilian Brunner, Eugenio Cuniato, Marco Tognon, and Roland Siegwart. Multi-directional Interaction Force Control with an Aerial Manipulator Under External Disturbances. *Autonomous Robots*, 47:1325–1343, 2023. doi: 10.1007/s10514-023-10128-2.
- [13] Gabriele Nava, Quentin Sablé, Marco Tognon, Daniele Pucci, and Antonio Franchi. Direct Force Feedback Control and Online Multi-Task Optimization for Aerial Manipulators. *IEEE Robotics and Automation Letters*, 5(2):331–338, 2020. doi: 10.1109/LRA.2019.2958473.
- [14] Alexandros Nikou, Georgios C. Gavridis, and Kostas J. Kyriakopoulos. Mechanical design, modelling and control of a novel aerial manipulator. In *2015 IEEE International Conference on Robotics and Automation (ICRA)*, pages 4698–4703, 2015. doi: 10.1109/ICRA.2015.7139851.
- [15] Anibal Ollero, Marco Tognon, Alejandro Suarez, Dongjun Lee, and Antonio Franchi. Past, Present, and Future of Aerial Robotic Manipulators. *IEEE Transactions on Robotics*, 38(1):626–645, 2022. doi: 10.1109/TRO.2021.3084395.
- [16] E.G. Papadopoulos and D.A. Rey. A new measure of tipover stability margin for mobile manipulators. In *Proceedings of IEEE International Conference on Robotics and Automation*, volume 4, pages 3111–3116 vol.4, 1996. doi: 10.1109/ROBOT.1996.509185.
- [17] Evangelos Papadopoulos and Daniel A. Rey. The Force-Angle Measure of Tipover Stability Margin for Mobile Manipulators. *Vehicle System Dynamics*, 33(1):29–48, 2000. doi: 10.1076/0042-3114(200001)33:1;1-5;FT029. URL <https://www.tandfonline.com/doi/abs/10.1076/0042-3114%28200001%2933%3A1%3B1-5%3BFT029>.
- [18] Sangyul Park, Jeongseob Lee, Joonmo Ahn, Myungsin Kim, Jongbeom Her, Gi-Hun Yang, and Dongjun Lee. ODAR: Aerial Manipulation Platform Enabling Omnidirectional Wrench Generation. *IEEE/ASME Transactions on Mechatronics*, 23(4):1907–1918, 2018. doi: 10.1109/TMECH.2018.2848255.
- [19] Lazar Peric, Maximilian Brunner, Karen Bodie, Marco Tognon, and Roland Siegwart. Direct Force and Pose NMPC with Multiple Interaction Modes for Aerial Push-and-Slide Operations. In *2021 IEEE International Conference on Robotics and Automation (ICRA)*, pages 131–137, 2021. doi: 10.1109/ICRA48506.2021.9561990.
- [20] Sujit Rajappa, Markus Ryll, Heinrich H. Bühlhoff, and Antonio Franchi. Modeling, control and design optimization for a fully-actuated hexarotor aerial vehicle with tilted propellers. In *2015 IEEE International Conference on Robotics and Automation (ICRA)*, pages 4006–4013, 2015. doi: 10.1109/ICRA.2015.7139759.
- [21] Ramy Rashad, Jelmer Goerres, Ronald Aarts, Johan B. C. Engelen, and Stefano Stramigioli. Fully Actuated Multirotor UAVs: A Literature Review. *IEEE Robotics & Automation Magazine*, 27(3):97–107, 2020. doi: 10.1109/MRA.2019.2955964.
- [22] Fabio Ruggiero, Jonathan Cacace, Hamid Sadeghian, and Vincenzo Lippiello. Passivity-based control of VTOL UAVs with a momentum-based estimator of external wrench and unmodeled dynamics. *Robotics and Autonomous Systems*, 72:139–151, 2015. ISSN 0921-8890. doi: <https://doi.org/10.1016/j.robot.2015.05>.

006. URL <https://www.sciencedirect.com/science/article/pii/S0921889015001049>.

- [23] S. Sugano, Q. Huang, and I. Kato. Stability criteria in controlling mobile robotic systems. In *Proceedings of 1993 IEEE/RSJ International Conference on Intelligent Robots and Systems (IROS '93)*, volume 2, pages 832–838 vol.2, 1993. doi: 10.1109/IROS.1993.583186.
- [24] Marco Tognon and Antonio Franchi. Omnidirectional Aerial Vehicles With Unidirectional Thrusters: Theory, Optimal Design, and Control. *IEEE Robotics and Automation Letters*, 3(3):2277–2282, 2018. doi: 10.1109/LRA.2018.2802544.
- [25] Marco Tognon, Hermes A. Tello Chávez, Enrico Gasparin, Quentin Sablé, Davide Bicego, Anthony Mallet, Marc Lany, Gilles Santi, Bernard Revaz, Juan Cortés, and Antonio Franchi. A Truly-Redundant Aerial Manipulator System With Application to Push-and-Slide Inspection in Industrial Plants. *IEEE Robotics and Automation Letters*, 4(2):1846–1851, 2019. doi: 10.1109/LRA.2019.2895880.
- [26] Miguel Ángel Trujillo, José Ramiro Martínez-de Dios, Carlos Martín, Antidio Viguria, and Aníbal Ollero. Novel Aerial Manipulator for Accurate and Robust Industrial NDT Contact Inspection: A New Tool for the Oil and Gas Inspection Industry. *Sensors*, 19(6), 2019. ISSN 1424-8220. doi: 10.3390/s19061305. URL <https://www.mdpi.com/1424-8220/19/6/1305>.
- [27] Robert Watson, Mina Kamel, Dayi Zhang, Gordon Dobie, Charles MacLeod, S. Gareth Pierce, and Juan Nieto. Dry Coupled Ultrasonic Non-Destructive Evaluation Using an Over-Actuated Unmanned Aerial Vehicle. *IEEE Transactions on Automation Science and Engineering*, 19(4):2874–2889, 2022. doi: 10.1109/TASE.2021.3094966.
- [28] Han W. Wopereis, Wilbert L. W. van de Ridder, Tom J. W. Lankhorst, Lucian Klooster, Evyatar M. Bukai, David Wuthier, George Nikolakopoulos, Stefano Stramigioli, Johan B. C. Engelen, and Matteo Fumagalli. Multimodal Aerial Locomotion: An Approach to Active Tool Handling. *IEEE Robotics & Automation Magazine*, 25(4):57–65, 2018. doi: 10.1109/MRA.2018.2869527.
- [29] Weixuan Zhang, Lionel Ott, Marco Tognon, and Roland Siegwart. Learning Variable Impedance Control for Aerial Sliding on Uneven Heterogeneous Surfaces by Proprioceptive and Tactile Sensing. *IEEE Robotics and Automation Letters*, 7(4):11275–11282, 2022. doi: 10.1109/LRA.2022.3194315.
- [30] Weixuan Zhang, Lionel Ott, Marco Tognon, and Roland Siegwart. Learning variable impedance control for aerial sliding on uneven heterogeneous surfaces by proprioceptive and tactile sensing. *IEEE Robotics and Automation Letters*, 7(4):11275–11282, 2022.
- [31] Suping Zhao, Fabio Ruggiero, Giuseppe Andrea Fontanelli, Vincenzo Lippiello, Zhanxia Zhu, and Bruno Siciliano. Nonlinear Model Predictive Control for the Stabilization of a Wheeled Unmanned Aerial Vehicle on a Pipe. *IEEE Robotics and Automation Letters*, 4(4):4314–4321, 2019. doi: 10.1109/LRA.2019.2931821.